OPTICS

Reconfigurable non-Hermitian soliton combs using dissipative couplings and topological windings

Seyed Danial Hashemi[1,2] and Sunil Mittal[1,2]*

The emergence of dissipative Kerr solitons in nonlinear resonators has revolutionized the generation of on-chip coherent optical frequency combs. The formation of dissipative Kerr solitons in conventional single resonators hinges on balancing the resonator dissipation against the parametric gain and balancing the resonator dispersion against the resonance frequency shifts introduced by the Kerr nonlinearity. Here, we theoretically introduce a previously unidentified class of non-Hermitian soliton combs that are enabled by engineering the dissipation and dispersion of a coupled resonator array with nonreciprocal couplings. We show that these non-Hermitian soliton combs allow unprecedented postfabrication agile reconfigurability of the soliton comb spectrum, where the number of comb lines, as well as their frequency spacing, can be markedly tuned by simply tuning the hopping phases between resonators. Such reconfigurable non-Hermitian combs generated using coupled resonator arrays could enable new functionalities for a multitude of comb applications.

INTRODUCTION

Dissipative Kerr solitons are pulses of light that preserve their shape when propagating in a dispersive and dissipative medium with Kerr nonlinearity. Dissipative Kerr solitons emerge naturally while generating coherent optical frequency combs in nonlinear resonators when the dissipation of the resonator is compensated for by the nonlinear gain and the dispersion of the resonator is compensated for by the dispersion induced by nonlinearity (*1*–*5*). Although engineering the resonator waveguide geometry is the most commonly used approach (*3*, *6*), recently techniques such as embedding photonic crystals or inverse-designed reflectors in ring resonators (*7*–*10*) and coupled resonator systems in the form of photonic molecules (*11*–*18*) have been explored to engineer the resonator dispersion and, therefore, the spatiotemporal behavior of Kerr soliton combs. More recently, large arrays of coupled resonators hosting topological edge states with linear dispersion have been shown to generate nested solitons and nested frequency combs that are not achievable using single resonators (*19*–*22*). Nevertheless, analogous advances in engineering the dissipation of the resonators to control the formation of soliton combs have remained largely elusive.

In parallel, recent advances in the field of non-Hermitian physics of open quantum systems have led to the development of a powerful paradigm that uses dissipation to engineer system behavior (*23*–*34*). In particular, non-Hermitian model systems, such as the Hatano-Nelson model with nonreciprocal couplings and open boundary conditions, exhibit the skin effect where all modes are exponentially localized at the boundary of the lattice (*23*–*25*, *32*, *35*–*37*). In systems with periodic boundaries, this non-Hermitian topology manifests itself as topologically nontrivial windings in the two-dimensional (2D) complex energy plane spanned by the real and imaginary eigenvalues (*32*, *37*–*39*). These windings reveal the intertwined nature of the dispersion (real eigenvalues) and dissipation (imaginary eigenvalues) of the non-Hermitian system where some of the modes experience higher dissipation than others.

Here, we theoretically introduce the paradigm of non-Hermitian optical frequency combs where we use engineered dissipation in a nonlinear system to enable the formation of Kerr solitons. Specifically, we consider an array of nonlinear ring resonators that are coupled using non-Hermitian dissipative couplings and nonzero hopping phases (a synthetic magnetic flux). By engineering the coupling strengths and hopping phases, we engineer the topological windings and, equivalently, the dispersion and dissipation of the supermodes of this array. We show that this simultaneous dissipation-dispersion engineering allows the formation of nested Kerr solitons and nested optical frequency combs (*19*–*21*) in the ring resonator array. These nested combs feature a comb-in-a-comb structure with comb lines repeating at two very different frequency scales. In the absence of such non-Hermitian engineering, this array will not support the formation of stable solitons because of undesired nonlinearity-induced mixing between the supermodes. Even more so, we show that non-Hermitian engineering allows the unprecedented postfabrication reconfigurability of the generated nested combs, where both the comb line spacing and the number of comb lines can be dynamically reconfigured by tuning the hopping phases (for example, using thermal heaters). Such extreme postfabrication reconfigurability is not achievable using conventional single-resonator Kerr combs, where the comb line spacing is set by the free spectral range (FSR) of the resonator.

Our results could lead to transformative changes in the applications of combs that span radio frequency signal synthesis and processing, frequency and time metrology, spectroscopy, and light detection and ranging and enable, for example, a reconfigurable platform for optical comb–based radio frequency signal synthesis and processing (*4*, *40*). On a more fundamental level, our results add the rich physics of frequency combs and temporal soliton formation to the growing field of nonlinear non-Hermitian systems, which have recently led to the demonstration of, for example, non-Hermitian spatial solitons (*41*), nonlinearity-controlled topological edge states and phase transitions (*31*, *42*–*44*), and non-Hermitian lasers (*45*, *46*).

Our system consists of a 1D array of site ring resonators arranged as a super-ring with periodic boundary conditions (Fig. 1A). The site rings are coupled to their nearest and next-nearest neighbors using another set of rings called the link rings (*47*, *48*). The resonance frequencies of the link rings are shifted from those of the site

[1]Department of Electrical and Computer Engineering, Northeastern University, Boston, MA 02115, USA. [2]Institute for NanoSystems Innovation, Northeastern University, Boston, MA 02115, USA.
*Corresponding author. Email: s.mittal@northeastern.edu

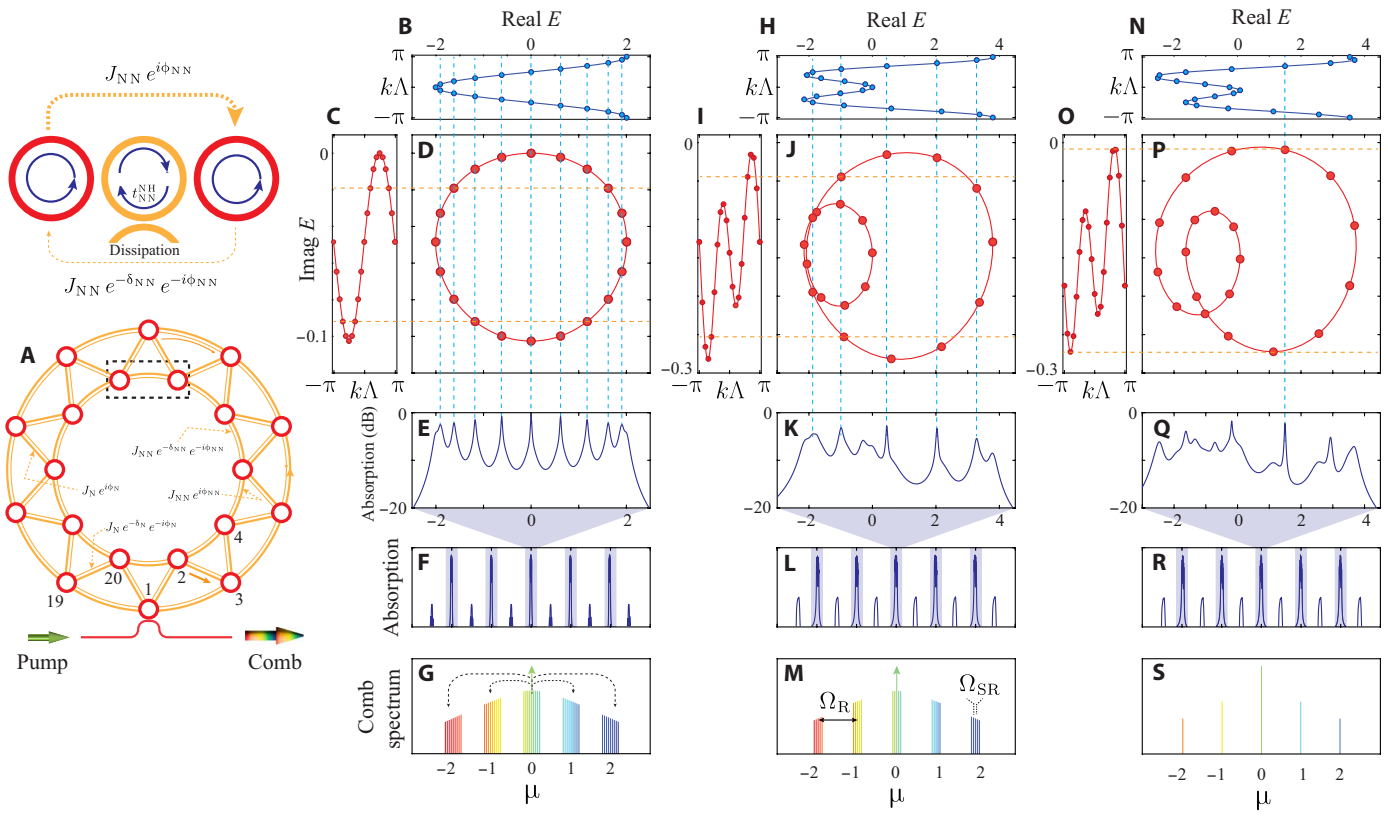

Fig. 1. Reconfigurable non-Hermitian soliton combs. (**A**) Schematic of the non-Hermitian array with site rings (shaded red and numbered as shown), dissipatively coupled to the nearest and next-nearest neighbors via link rings (shaded orange). The zoom-in shows an external waveguide coupled to the link ring that creates the dissipative couplings. The array is coupled to an input-output waveguide to inject pump light and out-couple generated comb. (**B** and **C**) Real and imaginary part of energy (frequency) eigenvalues, for a system with only nearest-neighbor couplings, as a function of Bloch momentum $k\Lambda$ in the array. Here, $J_N = 1, J_{NN} = 0, t_N^{NH} = 0.95$, and $\phi_N = \phi_{NN} = 0$. (**D**) Real and imaginary parts of eigenvalues plotted on a 2D complex plane show topological windings, here in the form of a circle. (**E**) Simulated absorption (1-transmission) spectrum of the linear array near a single FSR of the site rings. (**F**) Absorption spectrum over multiple FSRs. The spectrum in (E) is a zoom-in near one FSR of the site rings. (**G**) Schematic of the generated nested comb spectrum with nine supermodes oscillating at each FSR (labeled by μ). (**H** to **M**) Corresponding results for a lattice with both nearest-neighbor and next-nearest-neighbor couplings, with $J_N = J_{NN} = 1, t_N^{NH} = 0.95, t_{NN}^{NH} = 0.9, \phi_N = 0$, and $\phi_{NN} = 0.50625(2\pi)$. We now observe a double winding in the 2D complex energy plane and an engineered absorption spectrum, resulting in a nested comb with only five supermodes oscillating in each FSR. (**N** to **S**) Corresponding results for a lattice with a different hopping phase such that $J_N = J_{NN} = 1, t_N^{NH} = 0.95, t_{NN}^{NH} = 0.9, \phi_N = 0$, and $\phi_{NN} = 0.41667(2\pi)$. In this case, the generated comb spectrum shows the oscillation of only a single supermode in each FSR μ.

rings by one-half FSR, for example, by decreasing their length. The use of an additional waveguide coupled to the link rings allows us to introduce non-Hermitian dissipative couplings such that the photons experience a direction-dependent loss when hopping between neighboring site rings (Fig. 1A). In this configuration, the effective coupling rate for photons hopping toward the right neighboring site rings (J_N, J_{NN}) differs from those hopping toward the left $(J_N\, e^{-\delta_N}, J_{NN}\, e^{-\delta_{NN}})$. The nonreciprocal part of the couplings $e^{-\delta_N}, e^{-\delta_{NN}}$ is dictated by the transmission coefficients t_N^{NH} and t_{NN}^{NH} of the dissipative coupling regions of the link rings (Fig. 1A). Therefore, this system is non-Hermitian when $\delta_N > 0$ and/or $\delta_{NN} > 0$ or, equivalently, when $t_N^{NH} < 1$ and/or $t_{NN}^{NH} < 1$. We note that the effective coupling strength in either direction can be decreased by appropriately choosing the position (up or down) of the coupling waveguide that introduces direction-dependent loss. Appropriately shifting the link rings also allows us to introduce a direction-dependent phase $(\pm\phi_N, \pm\phi_{NN})$ when the photons hop between neighboring site rings (*47*, *48*). The simultaneous presence of direction-dependent hopping phases and hopping loss effectively creates both real and imaginary synthetic magnetic fields for photons. The array is coupled to an input-output waveguide at one of the site rings, which allows injection of a pump laser and out-coupling of the generated frequency comb.

We use the transfer-matrix formalism to calculate the frequency (energy) eigenvalues of this periodic, linear system as a function of the Bloch momentum k. The eigenvalues are calculated near a given longitudinal mode of single-ring resonators such that $\omega_{0,\mu}$ is the resonance frequency of the longitudinal mode labeled μ, and we set $\omega_{0,0} = 0$. The eigenvalues are presented in Fig. 1 for different choices of hopping strengths and hopping phases. In general, we note that the eigenvalues are complex. The real part of these eigenvalues represents the resonance frequencies and, therefore, the dispersion of the supermodes. Their imaginary part, which is always ≤ 0, represents the effective dissipation of the supermodes. We find that some of the supermodes experience much higher dissipation compared to others.

To reveal the interplay between the dispersion and dissipation of this non-Hermitian periodic system, we plot the real and imaginary

eigenvalues on a 2D complex plane, as shown in Fig. 1 (D, J, and P). In particular, we observe the emergence of topologically nontrivial closed-loop windings that govern the symmetries of the system with respect to the dispersion and dissipation of its supermodes (*32*, *37*–*39*). For example, for a system with only nearest-neighbor couplings $(J_{NN} = 0)$ and no hopping phases $(\phi_N = \phi_{NN} = 0)$, the topological winding is in the form of a circle such that the resonance frequencies (real eigenvalues) of the supermodes are located symmetrically around the ring resonance frequency $\omega_{0,0}$ (which we set to zero). Furthermore, the supermodes are twofold degenerate in their real part. The presence of dissipative couplings breaks this degeneracy in their imaginary part such that the supermode with momentum $-k$ experiences higher dissipation compared to the one with momentum $+k$ (Fig. 1C). By introducing next-nearest-neighbor couplings and hopping phases, we can introduce higher-order topological windings that can break these symmetries.

This eigenvalue structure is also manifested in the absorption (1-transmission) spectrum of the array, where we consider injecting light at the input and measuring the transmission at the output of the input-output waveguide. In particular, the frequencies at which we observe peaks in the absorption spectrum correspond to the real part of the eigenvalues. Similarly, we observe higher absorption in the array, through the input-output waveguide, for supermodes that have lower loss (or lower absolute imaginary eigenvalues). Evidently, by tuning hopping strengths, hopping phases, and the dissipation in the link rings, we can engineer the windings or, equivalently, both the dispersion and dissipation of the supermodes and their absorption spectra.

To generate frequency combs in the lattice, we consider a continuous-wave pump coupled to the lattice via the input-output waveguide. The pump generates the frequency comb via the nonlinear four-wave mixing (FWM) process. The number of supermodes participating in the generated comb spectra is controlled by both their real and imaginary eigenvalues. In particular, the real part of the eigenvalues dictates the supermode dispersion or energy conservation in the FWM process. The imaginary part of the eigenvalues dictates the balance between the loss introduced by dissipative couplings and the gain introduced by the FWM process. Therefore, only the supermodes that exhibit low loss (higher absorption) and are located approximately symmetrically around the pumped supermode contribute to the formation of coherent soliton combs. In the following, we will show that non-Hermitian engineering using dissipative couplings enables the formation of reconfigurable Kerr solitons and coherent optical frequency combs by selectively dissipating a set of supermodes and thereby suppressing undesired nonlinear mixing between the supermodes.

To simulate the generation of frequency combs, we use Ikeda map formalism as detailed in the Supplementary Materials (*49*–*51*). We emphasize that the commonly used Lugiato-Lefever formalism, which relies on the single-mode approximation and the effective Hamiltonian formalism, is not well suited for these simulations (*51*–*53*). This is because of the spurious gain terms introduced by the non-Hermitian couplings when using the single-mode approximation (see the Supplementary Materials). For our Ikeda map simulations, we use dimensionless normalized parameters such that the group velocity v_g, the length of the site rings L_R, and their FSR $\Omega_R/(2\pi)$ (in frequency units) are normalized to one. The coupling strength $J = 0.01\Omega_R$, and the loss rate of individual rings $\kappa_{in} = 0.01J$. We assume an anomalous dispersion for the ring resonators, represented by the parameter $D_2 = 5 \times 10^{-6}\Omega_R$. We do not make any assumptions regarding the dispersion or dissipation of the supermodes.

RESULTS

Comb in lattices with only nearest-neighbor couplings

To demonstrate the use of non-Hermitian dissipative couplings to control the formation of soliton combs, in Fig. 2, we first present results for the super-ring with $N = 20$ site rings, with only the nearest-neighbor couplings $J_N = J$, and all hopping phases set to zero ($\phi_N = \phi_{NN} = 0$). As discussed earlier, without dissipative couplings, such a system exhibits a twofold degeneracy in its eigenvalues (Figs. 1B and 2A). One supermode of this pair circulates the super-ring in the clockwise (CW) direction and the other in the counterclockwise (CCW) direction. This degeneracy is also evident in the absorption spectrum of the array, where only $\sim N/2$ modes are visible as absorption peaks (Fig. 2B). For a Hermitian system, all the eigenvalues are real, and it has a trivial topology (a line). Pumping the Hermitian super-ring at a single lattice site excites an equal superposition of both modes, and this competition hinders the formation of coherent soliton combs in the Hermitian super-ring array.

Nevertheless, as evident from Fig. 2A, the introduction of dissipative couplings with $t_N^{NH} = 0.95$ introduces nontrivial topological winding in the form of a circle. Although the supermodes stay doubly degenerate in their real eigenvalues, dissipative couplings break their degeneracy in the imaginary eigenvalues and suppress mixing between the CW and CCW propagating supermodes. For our choice of circulation direction in the site rings and the dissipative waveguide coupling in the link rings (Fig. 1A), supermodes with momentum $-k$, traveling in the CW direction around the super-ring, have higher loss than those traveling along the positive k (CCW) direction. The absorption spectrum of the non-Hermitian lattice is shown in Fig. 2B, where we observe an increase in the linewidth of the supermodes because of dissipative couplings. We have also included intraresonator dissipation, with rate $\kappa_{in} = 0.01J$, in both the site and the link rings.

To generate coherent soliton combs, we pump the supermode at the center of the absorption spectrum shown in Fig. 2B and analyze the spatiotemporal and spectral response of the array. When we tune the amplitude of the normalized pump field $E_{in} = 0.021$ and the pump frequency detuning $\delta\omega_p = \omega_p - \omega_{0,0} = -0.10005J$, in the spatiotemporal domain (Fig. 2D), we observe the formation of coherent nested solitons in the lattice, similar to those observed in 2D topological ring resonator arrays (*20*, *21*, *54*). In this state, the super-ring hosts a single supersoliton—a set of a few consecutive site rings, each of which also hosts a single soliton. The solitons within the site rings self-organize such that their position within the single rings is always the same, that is, they are phase locked. As time evolves, this nested soliton structure circulates the lattice in the CCW direction but without losing its coherence (also see movie S1). We do not observe any propagation in the CW direction. This indicates that none of the CW propagating modes participate in the comb formation because the nonlinear FWM gain is not sufficient to overcome their higher loss introduced by dissipative couplings.

This formation of a nested soliton in the lattice is manifested at the output of the lattice as the generation of nested pulses or bursts of light pulses (inset of Fig. 2E). The bursts are separated in time by

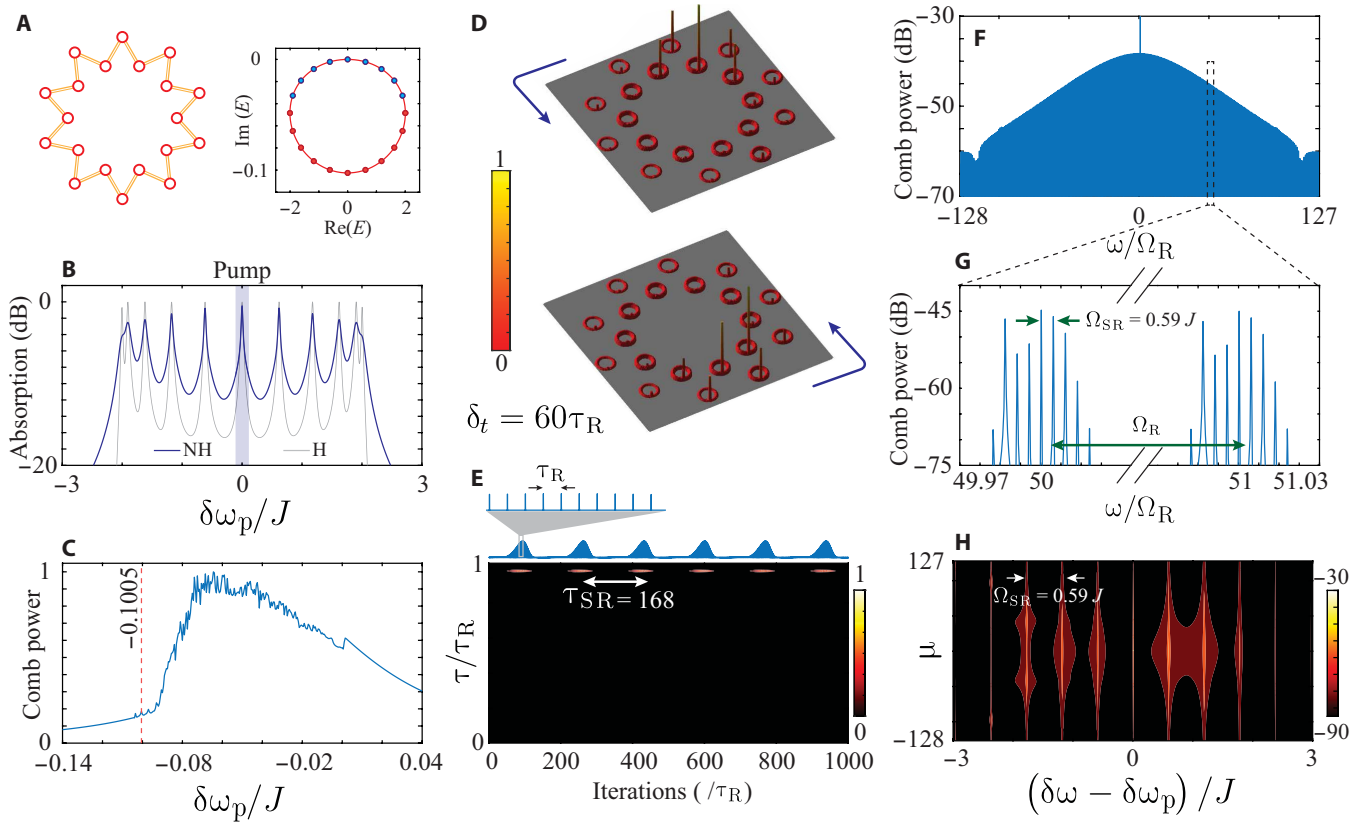

Fig. 2. Soliton combs in resonator arrays with only nearest-neighbor couplings. (**A**) Schematic of the array and the resultant winding in the form of a circle. The blue-shaded dots on the winding curve indicate supermodes that contribute to the nested comb formation. (**B**) Linear absorption (1-transmission) spectrum of the array for Hermitian and non-Hermitian lattices. The pumped mode is shaded blue. (**C**) Comb power as a function of pump frequency. The pump frequency where we observe nested solitons is indicated by the dashed line. (**D**) Soliton intensity distribution and its circulation around the array in the CCW direction. For clarity, the plot only shows the site rings. (**E**) Temporal output showing bursts of pulses, with each burst separated by the round-trip time $\tau_{SR} \simeq 168\tau_R$ of the super-ring. Within each burst, the light pulses are separated by the round-trip time τ_R of the single rings. (**F**) Generated comb spectrum and (**G**) zoom-in of the spectrum around FSRs $\mu = 50$ and $\mu = 51$. We observe the formation of a nested comb with the oscillation of nine supermodes in each FSR (similar to the schematic of Fig. 1G). The FSR of the subcomb $\Omega_{SR} = 1/\tau_{SR} = 0.59J = 0.0059\Omega_R$. (**H**) Comb spectrum reorganized as a function of fast (μ) and slow $\delta\omega$ frequency. The nested comb lines are straight, indicating cancellation of linear and nonlinear dispersion and formation of a soliton nested comb.

the round-trip time $\tau_{SR} \sim 168\tau_R$ of the super-ring resonator. Within each burst, the pulses are separated by the round-trip time τ_R of the single rings. The temporal output of the lattice, presented in Fig. 2E as a function of the fast time $\tau = (0, \tau_R)$ and the slow time (number of round trips or iterations), shows that pulses always appear at the same fast time τ. This highlights the phase-locked nature of the solitons within individual rings (Fig. 2D).

The generated frequency comb spectrum for this array is shown in Fig. 2F. The intensity profile across the comb lines is smooth, which indicates the formation of a coherent soliton comb. In Fig. 2G, we plot the comb spectrum zoomed in on two FSRs ($\mu = 50, 51$). We clearly observe the formation of a nested comb (Fig. 2, F to H) where predominantly a set of nine supermodes oscillates at each FSR μ. The different sets of oscillating supermodes are spaced by the FSR Ω_R of the single rings. The frequency spacing between consecutive supermodes within a single set is much smaller such that $\Omega_{SR} = 1/\tau_{SR} \simeq 0.59J = 0.0059\Omega_R$. We note that the number of oscillating modes (here, nine) is dictated by the dispersion and dissipation of the array as depicted by its topological winding, where we find a set of nine modes that have a lower loss (indicated by dashed lines in Fig. 1D) and are located symmetrically around the pumped mode.

To further highlight the soliton nature of this comb, in Fig. 2H, we plot the comb spectrum as a function of the longitudinal mode index μ of the single rings (which we refer to as the fast frequency) and the pump-normalized slow frequency $\delta\omega - \delta\omega_p = (\omega - \omega_{0,\mu}) - (\omega_p - \omega_{0,0})$, which reveals the oscillating supermodes within each FSR. Here, $\omega_{0,\mu}$ is the resonance frequency of μth FSR (of single rings), and $\omega_{0,0}$ with $\mu = 0$ is that for the pumped FSR. ω corresponds to the frequency of an oscillating supermode. We find that the nested comb lines do not show any curvature, which clearly indicates the cancellation of linear and nonlinear dispersion and the formation of coherent solitons. This spatiotemporal response and frequency comb spectrum of nested soliton combs can be contrasted with that of chaotic combs (see fig. S5), where we clearly observe the absence of a smooth comb spectrum, the underlying linear dispersion of the cavity manifested as the curvature of the generated comb lines, and the absence of stable spatial or temporal pattern formation.

Combs in lattices with nearest-neighbor and next-nearest-neighbor couplings

Next, we demonstrate the use of higher-order non-Hermitian topological windings to engineer the comb spectrum. Specifically, we introduce next-nearest-neighbor couplings J_{NN} and set their strength such that $J_{NN} = J_N = J$. We chose nonreciprocal couplings for both nearest and next-nearest neighbors such that $t_N^{NH} = 0.95$ and $t_{NN}^{NH} = 0.9$. We also introduce next-nearest-neighbor hopping phases $\phi_{NN} = 0.50625(2\pi)$. As shown in Fig. 3A, this system exhibits a non-Hermitian topology with double winding. The absorption spectrum for this system is shown in Fig. 3B and is compared to that of a Hermitian system. We note that because of next-nearest-neighbor couplings, the range of real eigenvalues $\sim(-2.5J, 4J)$ is much larger compared to the super-ring with only nearest-neighbor couplings, where this range was $\sim(-2J, 2J)$. The presence of the hopping phase ϕ_{NN} lifts the degeneracy in the real eigenvalues, and the Hermitian spectrum exhibits $N = 20$ peaks. However, the eigenvalues are nonuniformly distributed across the frequency spectrum. This nonuniformity can also be observed in the asymmetric location of the smaller winding loop in Fig. 3A. This skewed dispersion and undesired couplings between closely spaced counterpropagating supermodes make it challenging to achieve soliton combs in the Hermitian lattice. By introducing dissipative couplings, we engineer the absorption spectrum such that only five supermodes, nearly equally spaced in frequency, exhibit lower dissipation and, consequently, higher absorption (highlighted by dashed lines in Fig. 1J and blue shaded dots in Fig. 3A).

To generate nested combs, we pump the supermode in the center of the spectrum with the highest absorption. When we tune the pump frequency $\delta\omega_p = 0.11J$ and set the normalized pump field $E_{in} = 0.11$, we observe the formation of a coherent comb characterized by a smooth intensity profile (Fig. 3F). Within each FSR (Fig. 3G), we now observe the oscillation of predominantly five supermodes that correspond to the low-loss supermodes of the absorption spectrum. This contrasts the super-ring with only nearest-neighbor couplings, where we observed the oscillation of nine supermodes. Furthermore, the spacing between the oscillating supermodes $\Omega_{SR} \simeq 1.32J$, which is much larger compared to that in Fig. 2 (G and H), where it was only about $0.59J$. As before, we observe the complete cancellation of linear supermode dispersion against that of nonlinear dispersion, indicating the formation of coherent soliton combs (Fig. 3H).

In the super-ring, we again observe the self-formation of phase-locked nested solitons, propagating around the lattice in the CCW

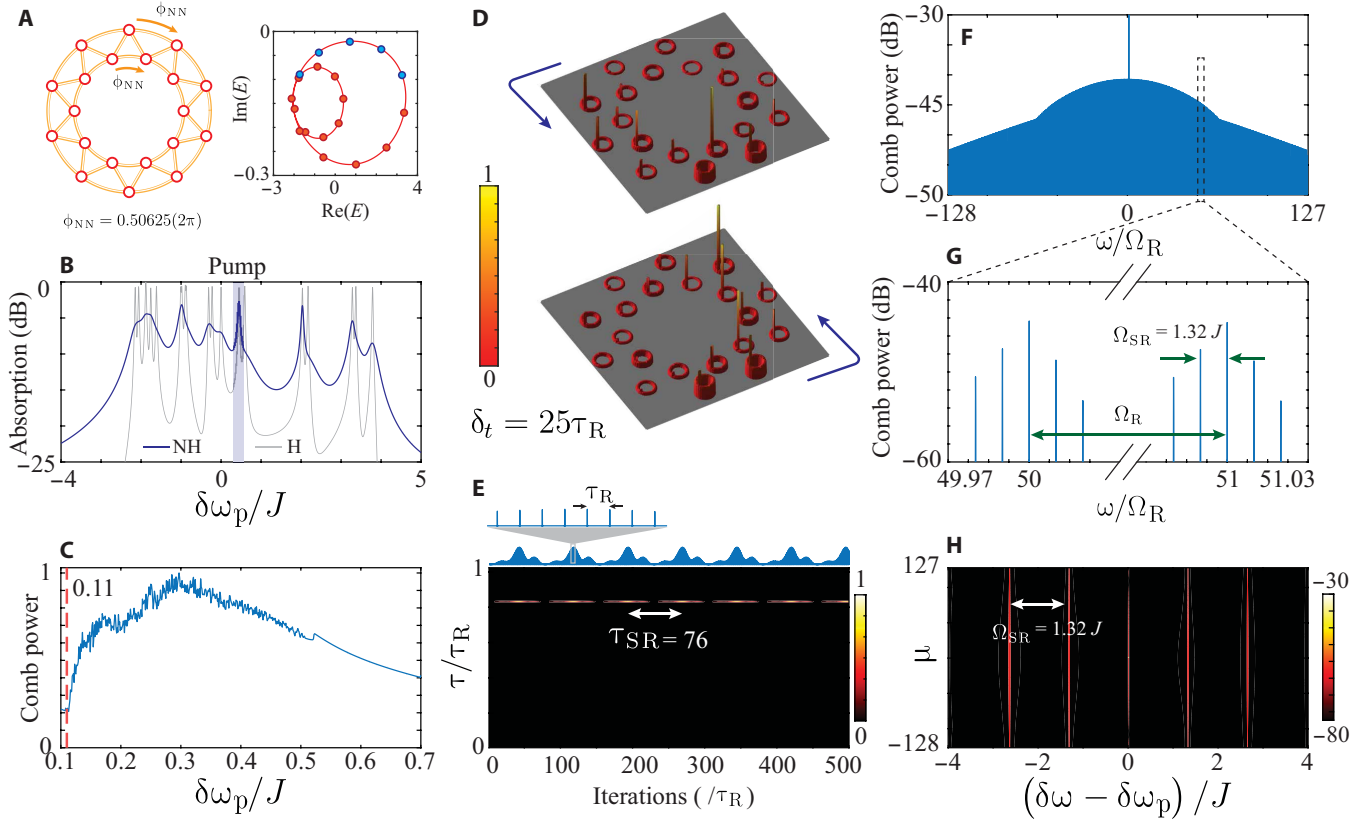

Fig. 3. Soliton combs in resonator arrays with nearest- and next-nearest-neighbor couplings, with phase $\phi_{NN} = 0.50625(2\pi)$, $J_N = J_{NN} = J$, $t_N^{NH} = 0.95$, and $t_{NN}^{NH} = 0.9$. (**A**) Schematic of the array and the resultant double winding. The blue-shaded dots on the winding curve indicate the low-dissipation supermodes that contribute to the nested comb formation. (**B**) Linear absorption spectrum of the array for Hermitian and non-Hermitian lattices. The supermodes with low dissipation manifest as prominent peaks in the spectrum. (**C**) Comb power as a function of pump frequency. The pump frequency where we observe nested solitons is indicated by the dashed line. (**D**) Soliton intensity distribution in the array. As before, the soliton position within each ring hosting the supersoliton is the same. With time, the nested soliton structure circulates the array in the CCW direction. (**E**) Temporal output showing bursts of pulses, with each burst separated by $\tau_{SR} \simeq 76\tau_R$. (**F** to **H**) Generated comb spectrum showing the oscillation of five supermodes at each FSR, with FSR $\Omega_{SR} = 1.32J$.

direction (Fig. 3D and movie S2). These are qualitatively similar to those observed in the super-ring with only nearest-neighbor couplings (Fig. 2D). The temporal output for this soliton comb also consists of bursts of pulses (Fig. 3E), but the periodicity of the bursts $\tau_{SR} = 76\tau_R$ is much smaller compared to that in Fig. 2, where it was $168\tau_R$. This decrease is consistent with the increase in the comb line spacing for next-nearest-neighbor combs. Nevertheless, we also observe secondary bursts in the temporal output that have exactly the same periodicity as that of the primary bursts. This is because of the oscillation of a fewer number of supermodes that increases the spatiotemporal width of nested solitons, that is, they occupy more site rings and, therefore, generate broader temporal pulses.

Tunability of the comb spectrum

While postfabrication tuning of the coupling rates between rings is challenging (*55*), the hopping phase can be tuned much more easily by, for example, incorporating thermal heaters on the link ring waveguides (*56*). To show that tuning the hopping phase can lead to the remarkable reconfigurability of the comb spectrum and the soliton state, in Fig. 4, we show results for a super-ring with the same coupling parameters as in Fig. 3, but we tune the hopping phase such that $\phi_{NN} = 0.41667(2\pi)$. In this case, the non-Hermitian topological winding number stays the same, but the position of the inner winding loop rotates in the 2D complex energy plane (Fig. 4A). The resulting absorption spectrum is shown in Fig. 4B. Although the spectrum exhibits multiple peaks with low loss, our deliberate choice of ϕ_{NN} ensures that the frequency spacing between the consecutive peaks is very different.

When we pump the highlighted supermode, at $\delta\omega_p = 0.72J$ and set pump field $E_{in} = 0.11$, we now observe the oscillation of only a single supermode in the comb spectrum (Fig. 4, F to H). This is in stark contrast with our previous demonstrations, where we observed nine and five supermodes in Figs. 2 and 3, respectively. This marked reduction in the number of oscillating supermodes is due to our choice of supermode dispersion: No three supermode resonances are equally spaced in frequency to satisfy energy conservation for the FWM process.

In the super-ring, we observe the formation of a soliton molecule state where each site ring exhibits a single soliton (Fig. 4D). As before, the solitons across different rings are phase locked. This soliton-molecule state is stationary and does not show any evolution/circulation with time (movie S3). This observation of a uniform spatial intensity distribution in the super-ring is consistent with the oscillation of a single supermode in the comb spectrum. The temporal

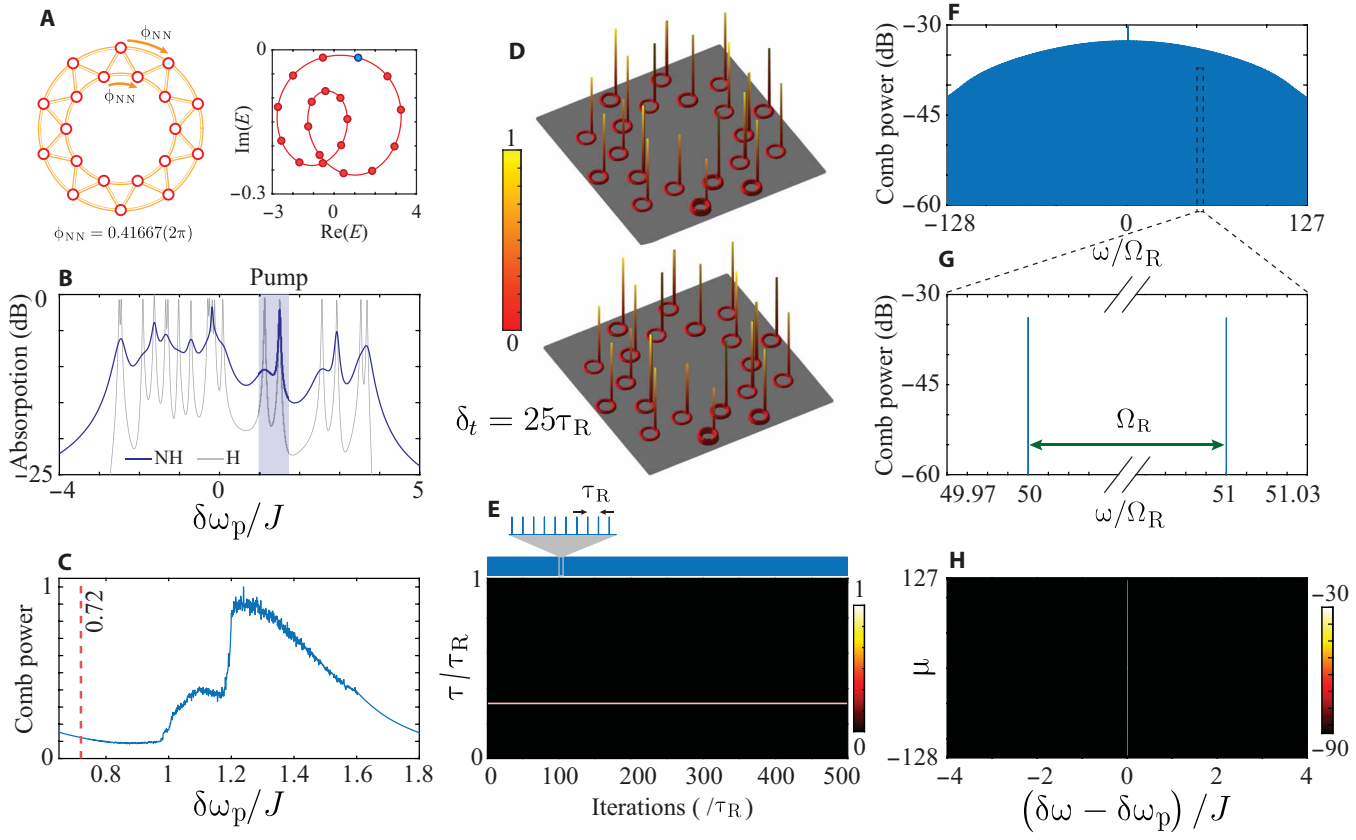

Fig. 4. Soliton combs in resonator arrays with nearest-neighbor and next-nearest-neighbor couplings, with phase $\phi_{NN} = 0.41667(2\pi)$, $J_N = J_{NN} = J$, $t_N^{NH} = 0.95$, and $t_{NN}^{NH} = 0.9$. (**A**) Schematic of the array and the resultant double winding. The blue-shaded dot on the winding curve indicates the pumped mode. (**B**) Linear absorption spectrum of the array. The frequency spacings between neighboring supermodes with low dissipation are very different, which prevents the oscillation of multiple modes in the comb spectrum. (**C**) Comb power as a function of pump frequency. (**D**) Soliton intensity distribution in the array. Each site ring of the array hosts exactly one soliton, and the soliton position within each ring is exactly the same. The soliton molecule structure does not show any evolution with time. (**E**) Temporal output showing the generation of periodic light pulses separated by τ_R. (**F** to **H**) Generated comb spectrum where we observe the oscillation of only a single supermode at each FSR.

output of this super-ring shows periodic pulses with a repetition rate of τ_R (Fig. 4E). There are no bursts of pulses as were observed with nested solitons. We note that this output temporal and frequency spectrum of this lattice is exactly the same as that of a single-ring resonator: comb lines separated by Ω_R and temporal pulses separated by $\tau_R = \frac{1}{\Omega_R}$. However, this spectrum is generated by a set of 20 self-synchronized ring resonators.

DISCUSSION

To summarize, we have demonstrated the use of dissipative couplings to engineer the generation of soliton combs in 1D resonator arrays with periodic boundary conditions. Although we have explored only a very small subset of parameter choices, this system offers many degrees of freedom in the form of relative strength of nearest and next-nearest couplings J_N / J_{NN}, relative phase ϕ_{NN} and ϕ_N, and even the strength of dissipation δ_N and δ_{NN}. The system could be designed using another choice of fixed parameters $(J_N, J_{NN}, \delta_N, \delta_{NN})$ such that tuning hopping phases could lead to even more marked agile reconfigurability of the comb spectrum. This operating regime could also be set to suit a particular comb application. As examples, in the Supplementary Materials, we show results for other parameter choices where we observe the formation of a nested comb with three and seven oscillating supermodes in each FSR.

Our approach is very general and can be easily extended to generate previously unobserved soliton comb states in 2D coupled ring resonator arrays where, for example, first-order or higher-order non-Hermitian physics could lead to topologically nontrivial states of light (*47*, *48*, *57*–*63*). Although we have focused on Kerr combs, non-Hermitian engineering can also be applied to engineer, for example, electro-optic or optomechanical combs (*64*–*67*). Therefore, our results pave the way to explore the rich synergy between nonlinear dynamics and the formation of frequency combs, synthetic dimensions, and the physics of driven dissipative non-Hermitian systems.

METHODS

Ikeda map formalism

The formation of dissipative Kerr solitons and coherent optical frequency combs in single and weakly coupled resonators can be efficiently simulated using the Lugiato-Lefever equations. However, this formalism relies on the single-mode approximation and the effective Hamiltonian approach, which leads to spurious gain for some of the supermodes of the non-Hermitian array, even when the linear system is completely passive with no gain (see the Supplementary Materials). The transmission and the winding spectrum of the array calculated using a transfer matrix–based approach show that all the supermodes experience loss because of the dissipative couplings. Nevertheless, depending on the coupling strengths, the hopping phases, and the dissipation strength in link rings, different supermodes experience very different effective losses. Therefore, to simulate the generation of soliton combs in our non-Hermitian array, we use Ikeda map formalism, which is inherently based on the transfer-matrix approach (*22*, *49*–*51*).

In Ikeda map formalism, the electric field $E_r^m(z,\tau)$ for a ring number r, where $r = (1, N)$, at a location z along the ring waveguide and at time $\tau = (0, \tau_R)$ is given as

$$\frac{dE_r^m(z,\mu)}{dz} = i\frac{2\pi}{L_R\Omega_R}\left(\omega_p + \Omega_R\mu - \omega_{0,\mu}\right)E_r^m(z,\mu) - \alpha E_r^m(z,\mu) + i\gamma\frac{1}{\tau_R}\int_0^{\tau_R} d\tau\,|E_r^m(z,\tau)|^2\,E_r^m(z,\tau)e^{i\omega_\mu\tau} \quad (1)$$

Here, m is the round-trip number such that any time $t = \tau + (m-1)\tau_R$. The Fourier transform of the field $E_r^m(z,\tau)$ with respect to the fast time τ yields $E_r^m(z,\mu)$, which is the field in the fast frequency domain indicated by the longitudinal mode index μ. $\gamma = 2\epsilon_0 n_0 n_2 \omega_0$ is the strength of Kerr nonlinearity (*68*), and $\alpha = \kappa_{in}/v_g$ is the propagation loss in the ring waveguides. For a lattice with both nearest and next-nearest couplings, we index the rings such that r = 1,4,7, … refer to the site rings, r = 2,5,8, … refer to the link rings connecting neighboring site rings, and r = 3,6,9, … refer to the link rings connecting next-nearest neighbor site rings. Therefore, for a lattice with $N = 20$ site rings, the array consists of a total of 60 rings when both the nearest and next-nearest couplings are present. We also account for the slightly different length of the link rings compared to those of the site rings.

We assume the individual ring resonators to have an anomalous dispersion such that they generate a bright comb. This dispersion is included in the ring resonance frequencies as

$$\omega_{0,\mu} = \omega_0 + \Omega_R\mu + \frac{D_2}{2}\mu^2 \quad (2)$$

where $\omega_0 = \omega_{0,0}$ is the resonance frequency of the pumped mode ($\mu = 0$), $\Omega_R = 2\pi\frac{v_g}{L_R}$ is the FSR (in angular frequency units), L_R is the length of the ring resonator, and D_2 is the second-order anomalous dispersion, which we assume to be $5 \times 10^{-6}\Omega_R$.

To further simplify the simulation framework, we use dimensionless parameters and normalize coordinates such that $z \to \frac{z}{L_R} = \{0, 1\}$, fast-time $\tau \to \frac{\tau}{\tau_R} = \{0, 1\}$, FSR $\Omega_R = 2\pi$, and the group velocity $v_g = 1$. Furthermore, the dimensionless fields $E_r^m(z,\tau) \to \sqrt{\gamma L}E_r^m(z,\tau)$ such that $\gamma = 1$ effectively. The nonlinear propagation is then written using the dimensionless parameters as

$$\frac{dE_r^m(z,\mu)}{dz} = i\left(\omega_p - \omega_0 - \frac{D_2}{2}\mu^2\right)E_r^m(z,\mu) - \alpha E_r^m(z,\mu) + i\int_0^1 d\tau\,|E_r^m(z,\tau)|^2\,E_r^m(z,\tau)e^{i\omega_\mu\tau} \quad (3)$$

Both the nearest-neighbor and next-nearest-neighbor couplings between the site rings are mediated by link rings. Each such coupling region between the site and the link rings is described as

$$\begin{bmatrix} E_r^m(z_c,\tau) \\ E_{r\prime}^m(z_c,\tau) \end{bmatrix} = \begin{pmatrix} t & i\kappa \\ i\kappa & t \end{pmatrix}\begin{bmatrix} E_r^m(z_c,\tau) \\ E_{r\prime}^m(z_c,\tau) \end{bmatrix} \quad (4)$$

Here, $t = t_N, t_{NN}$, and $\kappa = \kappa_N, \kappa_{NN}$ are the transmission and coupling coefficients for nearest-neighbor and next-nearest-neighbor couplings between rings indexed r and r', respectively.

The dissipative coupling region of the link rings is modeled as

$$E_r^m(z_{NH},\tau) = t^{NH}E_r^m(z_{NH},\tau) \quad (5)$$

where $t^{NH} = t_N^{NH}, t_{NN}^{NH}$ dictates the transmission/loss in the link ring section for nearest-neighbor and next-neighbor couplings, respectively. z_{NH} refers to the location of the link rings where we introduce the non-Hermitian coupling waveguide.

The coupling of the input-output waveguide to the lattice at location $r = 1$ is similarly described using coupling coefficient κ_{IO} such that

$$E_{out}^m(\tau) = i\kappa_{IO}E_1^m(z=1,\tau) + t_{IO}E_{in}(\tau) \quad (6)$$

Here, $E_{in}(\tau)$ is the input pump field, and $E_{out}^m(\tau)$ is the output field. This field $E_{out}^m(\tau)$ yields the temporal output of the generated frequency comb at any time $t = (m-1)\tau_R + \tau$, and its Fourier transform yields the frequency spectrum $E_{out}(\omega)$. The coupling coefficient κ_{IO} is related to the input-output coupling strength $\kappa_{ex} = \frac{\kappa_{IO}^2}{2}\frac{v_g}{L_R}$, where v_g is the group velocity. For our simulations, we chose $\kappa_{ex} = 0.1J$. Our choice of normalized device parameters, for example, an FSR $\Omega_R/(2\pi) = 250\,\text{GHz}$, $J/(2\pi) = 2.5\,\text{GHz}$, $\kappa_{in}/(2\pi) = 25\,\text{MHz}$, and $D_2/(2\pi) = 1.250\,\text{MHz}$ can be achieved using low-loss silicon-nitride resonators (*69*). For these parameters, the required pump power $P_{in} = \frac{c}{n_2\omega_0 L_R}A_{eff}|E_{in}|^2 \simeq 0.8\,\text{W}$ to generate soliton combs in the nearest-neighbor coupled device and $P_{in} = \sim 20\,\text{W}$ for the next-nearest-neighbor coupled devices. Nevertheless, the required pump power could be substantially reduced by reducing the inter-resonator coupling strength J, that is, increasing the loaded quality factor of the rings and also by optimizing the input-output coupling strength κ_{ex}.

Supplementary Materials

The PDF file includes:
Supplementary Text
Figs. S1 to S5
Legends for movies S1 to S3

Other Supplementary Material for this manuscript includes the following:
Movies S1 to S3

REFERENCES AND NOTES

1. S. T. Cundiff, J. Ye, *Colloquium*: Femtosecond optical frequency combs. *Rev. Mod. Phys.* **75**, 325–342 (2003).
2. T. J. Kippenberg, R. Holzwarth, S. A. Diddams, Microresonator-based optical frequency combs. *Science* **332**, 555–559 (2011).
3. T. J. Kippenberg, A. L. Gaeta, M. Lipson, M. L. Gorodetsky, Dissipative Kerr solitons in optical microresonators. *Science* **361**, eaan8083 (2018).
4. A. Pasquazi, M. Peccianti, L. Razzari, D. J. Moss, S. Coen, M. Erkintalo, Y. K. Chembo, T. Hansson, S. Wabnitz, P. Del'Haye, X. Xue, A. M. Weiner, R. Morandotti, Micro-combs: A novel generation of optical sources. *Phys. Rep.* **729**, 1–81 (2018).
5. A. L. Gaeta, M. Lipson, T. J. Kippenberg, Photonic-chip-based frequency combs. *Nat. Photonics* **13**, 158–169 (2019).
6. M. H. Anderson, W. Weng, G. Lihachev, A. Tikan, J. Liu, T. J. Kippenberg, Zero dispersion Kerr solitons in optical microresonators. *Nat. Commun.* **13**, 4764 (2022).
7. S.-P. Yu, D. C. Cole, H. Jung, G. T. Moille, K. Srinivasan, S. B. Papp, Spontaneous pulse formation in edgeless photonic crystal resonators. *Nat. Photonics* **15**, 461–467 (2021).
8. S.-P. Yu, E. Lucas, J. Zang, S. B. Papp, A continuum of bright and dark-pulse states in a photonic-crystal resonator. *Nat. Commun.* **13**, 3134 (2022).
9. E. Lucas, S.-P. Yu, T. C. Briles, D. R. Carlson, S. B. Papp, Tailoring microcombs with inverse-designed, meta-dispersion microresonators. *Nat. Photonics* **17**, 943–950 (2023).
10. J. Yang, M. A. Guidry, D. M. Lukin, K. Yang, J. Vučković, Inverse-designed silicon carbide quantum and nonlinear photonics. *Light Sci. Appl.* **12**, 201 (2023).
11. S. A. Miller, Y. Okawachi, S. Ramelow, K. Luke, A. Dutt, A. Farsi, A. L. Gaeta, M. Lipson, Tunable frequency combs based on dual microring resonators. *Opt. Express* **23**, 21527–21540 (2015).
12. S. Kim, K. Han, C. Wang, J. A. Jaramillo-Villegas, X. Xue, C. Bao, Y. Xuan, D. E. Leaird, A. M. Weiner, M. Qi, Dispersion engineering and frequency comb generation in thin silicon nitride concentric microresonators. *Nat. Commun.* **8**, 372 (2017).
13. J. K. Jang, A. Klenner, X. Ji, Y. Okawachi, M. Lipson, A. L. Gaeta, Synchronization of coupled optical microresonators. *Nat. Photonics* **12**, 688–693 (2018).
14. J. P. Vasco, V. Savona, Slow-light frequency combs and dissipative Kerr solitons in coupled-cavity waveguides. *Phys. Rev. Appl.* **12**, 064065 (2019).
15. Ó. B. Helgason, F. R. Arteaga-Sierra, Z. Ye, K. Twayana, P. A. Andrekson, M. Karlsson, J. Schröder, V. Torres-Company, Dissipative solitons in photonic molecules. *Nat. Photonics* **15**, 305–310 (2021).
16. A. Tikan, J. Riemensberger, K. Komagata, S. Hönl, M. Churaev, C. Skehan, H. Guo, R. N. Wang, J. Liu, P. Seidler, T. J. Kippenberg, Emergent nonlinear phenomena in a driven dissipative photonic dimer. *Nat. Phys.* **17**, 604–610 (2021).
17. Z. Yuan, M. Gao, Y. Yu, H. Wang, W. Jin, Q.-X. Ji, A. Feshali, M. Paniccia, J. Bowers, K. Vahala, Soliton pulse pairs at multiple colours in normal dispersion microresonators. *Nat. Photonics* **17**, 977–983 (2023).
18. Ó. B. Helgason, M. Girardi, Z. Ye, F. Lei, J. Schröder, V. Torres-Company, Surpassing the nonlinear conversion efficiency of soliton microcombs. *Nat. Photonics* **17**, 992–999 (2023).
19. S. Mittal, G. Moille, K. Srinivasan, Y. K. Chembo, M. Hafezi, Topological frequency combs and nested temporal solitons. *Nat. Phys.* **17**, 1169–1176 (2021).
20. C. J. Flower, M. Jalali Mehrabad, L. Xu, G. Moille, D. G. Suarez-Forero, O. Örsel, G. Bahl, Y. Chembo, K. Srinivasan, S. Mittal, M. Hafezi, Observation of topological frequency combs. *Science* **384**, 1356–1361 (2024).
21. A. Tusnin, A. Tikan, K. Komagata, T. J. Kippenberg, Nonlinear dynamics and Kerr frequency comb formation in lattices of coupled microresonators. *Commun. Phys.* **6**, 317 (2023).
22. S. D. Hashemi, S. Mittal, Floquet topological dissipative Kerr solitons and incommensurate frequency combs. *Nat. Commun.* **15**, 9642 (2024).
23. Z. Gong, Y. Ashida, K. Kawabata, K. Takasan, S. Higashikawa, M. Ueda, Topological phases of non-Hermitian systems. *Phys. Rev. X* **8**, 031079 (2018).
24. Y. Ashida, Z. Gong, M. Ueda, Non-Hermitian physics. *Adv. Phys.* **69**, 249–435 (2020).
25. N. Okuma, K. Kawabata, K. Shiozaki, M. Sato, Topological origin of non-Hermitian skin effects. *Phys. Rev. Lett.* **124**, 086801 (2020).
26. K. Kawabata, K. Shiozaki, M. Ueda, M. Sato, Symmetry and topology in non-Hermitian physics. *Phys. Rev. X* **9**, 041015 (2019).
27. N. Okuma, M. Sato, Non-Hermitian topological phenomena: A review. *Annu. Rev. Condens. Matter Phys.* **14**, 83–107 (2023).
28. R. El-Ganainy, K. G. Makris, M. Khajavikhan, Z. H. Musslimani, S. Rotter, D. N. Christodoulides, Non-Hermitian physics and PT symmetry. *Nat. Phys.* **14**, 11–19 (2018).
29. M.-A. Miri, A. Alù, Exceptional points in optics and photonics. *Science* **363**, eaar7709 (2019).
30. H. Nasari, G. G. Pyrialakos, D. N. Christodoulides, M. Khajavikhan, Non-Hermitian topological photonics. *Opt. Mater. Express* **13**, 870 (2023).
31. Z. Li, C. Li, G. Xu, W. Chen, Z. Xiong, H. Jing, J. S. Ho, C.-W. Qiu, Synergetic positivity of loss and noise in nonlinear non-Hermitian resonators. *Sci. Adv.* **9**, eadi0562 (2023).
32. Q. Wang, Y. D. Chong, Non-Hermitian photonic lattices: Tutorial. *J. Opt. Soc. Am. B* **40**, 1443–1466 (2023).
33. K. Fang, J. Luo, A. Metelmann, M. H. Matheny, F. Marquardt, A. A. Clerk, O. Painter, Generalized non-reciprocity in an optomechanical circuit via synthetic magnetism and reservoir engineering. *Nat. Phys.* **13**, 465–471 (2017).
34. A. Metelmann, A. A. Clerk, Nonreciprocal photon transmission and amplification via reservoir engineering. *Phys. Rev. X* **5**, 021025 (2015).
35. S. Weidemann, M. Kremer, T. Helbig, T. Hofmann, A. Stegmaier, M. Greiter, R. Thomale, A. Szameit, Topological funneling of light. *Science* **368**, 311–314 (2020).
36. C. Leefmans, A. Dutt, J. Williams, L. Yuan, M. Parto, F. Nori, S. Fan, A. Marandi, Topological dissipation in a time-multiplexed photonic resonator network. *Nat. Phys.* **18**, 442–449 (2022).
37. K. Ding, C. Fang, G. Ma, Non-Hermitian topology and exceptional-point geometries. *Nat. Rev. Phys.* **4**, 745–760 (2022).
38. K. Wang, A. Dutt, K. Y. Yang, C. C. Wojcik, J. Vučković, S. Fan, Generating arbitrary topological windings of a non-Hermitian band. *Science* **371**, 1240–1245 (2021).
39. K. Wang, A. Dutt, C. C. Wojcik, S. Fan, Topological complex-energy braiding of non-Hermitian bands. *Nature* **598**, 59–64 (2021).
40. Y. K. Chembo, Kerr optical frequency combs: Theory, applications and perspectives. *Nanophotonics* **5**, 214–230 (2016).
41. N. Pernet, P. St-Jean, D. D. Solnyshkov, G. Malpuech, N. Carlon Zambon, Q. Fontaine, B. Real, O. Jamadi, A. Lemaître, M. Morassi, L. Le Gratiet, T. Baptiste, A. Harouri, I. Sagnes, A. Amo, S. Ravets, J. Bloch, Gap solitons in a one-dimensional driven-dissipative topological lattice. *Nat. Phys.* **18**, 678–684 (2022).

42. S. Xia, D. Kaltsas, D. Song, I. Komis, J. Xu, A. Szameit, H. Buljan, K. G. Makris, Z. Chen, Nonlinear tuning of PT symmetry and non-Hermitian topological states. *Science* **372**, 72–76 (2021).
43. T. Dai, Y. Ao, J. Mao, Y. Yang, Y. Zheng, C. Zhai, Y. Li, J. Yuan, B. Tang, Z. Li, J. Luo, W. Wang, X. Hu, Q. Gong, J. Wang, Non-Hermitian topological phase transitions controlled by nonlinearity. *Nat. Phys.* **20**, 101–108 (2024).
44. M. Reisenbauer, H. Rudolph, L. Egyed, K. Hornberger, A. V. Zasedatelev, M. Abuzarli, B. A. Stickler, U. Delić, Non-Hermitian dynamics and non-reciprocity of optically coupled nanoparticles. *Nat. Phys.* **20**, 1629–1635 (2024).
45. Y. G. N. Liu, Y. Wei, O. Hemmatyar, G. G. Pyrialakos, P. S. Jung, D. N. Christodoulides, M. Khajavikhan, Complex skin modes in non-Hermitian coupled laser arrays. *Light Sci. Appl.* **11**, 336 (2022).
46. C. R. Leefmans, M. Parto, J. Williams, G. H. Y. Li, A. Dutt, F. Nori, A. Marandi, Topological temporally mode-locked laser. *Nat. Phys.* **20**, 852–858 (2024).
47. M. Hafezi, E. A. Demler, M. D. Lukin, J. M. Taylor, Robust optical delay lines with topological protection. *Nat. Phys.* **7**, 907–912 (2011).
48. M. Hafezi, S. Mittal, J. Fan, A. Migdall, J. Taylor, Imaging topological edge states in silicon photonics. *Nat. Photonics* **7**, 1001–1005 (2013).
49. K. Ikeda, Multiple-valued stationary state and its instability of the transmitted light by a ring cavity system. *Opt. Commun.* **30**, 257–261 (1979).
50. T. Hansson, S. Wabnitz, Frequency comb generation beyond the Lugiato–Lefever equation: Multi-stability and super cavity solitons. *J. Opt. Soc. Am. B* **32**, 1259–1266 (2015).
51. T. Hansson, S. Wabnitz, Dynamics of microresonator frequency comb generation: Models and stability. *Nanophotonics* **5**, 231–243 (2016).
52. B. E. Little, S. T. Chu, H. A. Haus, J. Foresi, J.-P. Laine, Microring resonator channel dropping filters. *J. Light. Technol.* **15**, 998–1005 (1997).
53. Y. K. Chembo, C. R. Menyuk, Spatiotemporal Lugiato-Lefever formalism for Kerr-comb generation in whispering-gallery-mode resonators. *Phys. Rev. A* **87**, 053852 (2013).
54. S. Mittal, V. V. Orre, E. A. Goldschmidt, M. Hafezi, Tunable quantum interference using a topological source of indistinguishable photon pairs. *Nat. Photonics* **15**, 542–548 (2021).
55. M. B. On, F. Ashtiani, D. Sanchez-Jacome, D. Perez-Lopez, S. J. B. Yoo, A. Blanco-Redondo, Programmable integrated photonics for topological Hamiltonians. *Nat. Commun.* **15**, 629 (2024).
56. S. Mittal, S. Ganeshan, J. Fan, A. Vaezi, M. Hafezi, Measurement of topological invariants in a 2D photonic system. *Nat. Photonics* **10**, 180–183 (2016).
57. S. Mittal, V. V. Orre, D. Leykam, Y. D. Chong, M. Hafezi, Photonic anomalous quantum hall effect. *Phys. Rev. Lett.* **123**, 043201 (2019).
58. S. Mittal, V. V. Orre, G. Zhu, M. A. Gorlach, A. Poddubny, M. Hafezi, Photonic quadrupole topological phases. *Nat. Photonics* **13**, 692–696 (2019).
59. S. Afzal, T. J. Zimmerling, Y. Ren, D. Perron, V. Van, Realization of anomalous floquet insulators in strongly coupled nanophotonic lattices. *Phys. Rev. Lett.* **124**, 253601 (2020).
60. T. Ozawa, T. Hayata, Two-dimensional lattice with an imaginary magnetic field. *Phys. Rev. B* **109**, 085113 (2024).
61. X.-W. Luo, C. Zhang, Higher-order topological corner states induced by gain and loss. *Phys. Rev. Lett.* **123**, 073601 (2019).
62. E. Edvardsson, F. K. Kunst, E. J. Bergholtz, Non-Hermitian extensions of higher-order topological phases and their biorthogonal bulk-boundary correspondence. *Phys. Rev. B* **99**, 081302 (2019).
63. T. Ozawa, H. M. Price, A. Amo, N. Goldman, M. Hafezi, L. Lu, M. C. Rechtsman, D. Schuster, J. Simon, O. Zilberberg, I. Carusotto, Topological photonics. *Rev. Mod. Phys.* **91**, 015006 (2019).
64. M. Zhang, B. Buscaino, C. Wang, A. Shams-Ansari, C. Reimer, R. Zhu, J. M. Kahn, M. Lončar, Broadband electro-optic frequency comb generation in a lithium niobate microring resonator. *Nature* **568**, 373–377 (2019).
65. A. Rueda, F. Sedlmeir, M. Kumari, G. Leuchs, H. G. L. Schwefel, Resonant electro-optic frequency comb. *Nature* **568**, 378–381 (2019).
66. J. Zhang, B. Peng, S. Kim, F. Monifi, X. Jiang, Y. Li, P. Yu, L. Liu, Y.-x. Liu, A. Alù, L. Yang, Optomechanical dissipative solitons. *Nature* **600**, 75–80 (2021).
67. H. M. E. Hussein, S. Kim, M. Rinaldi, A. Alù, C. Cassella, Passive frequency comb generation at radiofrequency for ranging applications. *Nat. Commun.* **15**, 2844 (2024).
68. R. W. Boyd, *Nonlinear Optics* (Academic Press Inc., ed. 3, 2008).
69. M. H. P. Pfeiffer, C. Herkommer, J. Liu, H. Guo, M. Karpov, E. Lucas, M. Zervas, T. J. Kippenberg, Octave-spanning dissipative Kerr soliton frequency combs in Si_3N_4 microresonators. *Optica* **4**, 684–691 (2017).

Acknowledgments

Funding: This research was supported by startup and TIER 1 grants from Northeastern University. **Author contributions:** S.M. conceived the idea and developed the simulation framework. S.D.H. performed the numerical simulations. Both authors contributed to the analysis of the data. S.D.H. and S.M. prepared the figures. S.M. wrote the manuscript with input from S.D.H. S.M. supervised the project. **Competing interests:** The authors declare that they have no competing interests. **Data and materials availability:** All data needed to evaluate the conclusions in the paper are present in the paper and/or the Supplementary Materials. Source data corresponding to the results reported in the manuscript are available on Dryad at the link https://doi.org/10.5061/dryad.np5hqc03z.

Submitted 15 November 2024
Accepted 21 April 2025
Published 28 May 2025
10.1126/sciadv.adu6554